RSC Advances

PAPER

View Article Online
View Journal | View Issue

Check for updates

Cite this: *RSC Adv.*, 2018, **8**, 7847

Compact TiO_2 films with sandwiched Ag nanoparticles as electron-collecting layer in planar type perovskite solar cells: improvement in efficiency and stability†

Seid Yimer Abate, [abc] Wen-Ti Wu, *[a] Someshwar Pola *[d] and Yu-Tai Tao *[a]

Received 29th December 2017
Accepted 13th February 2018

DOI: 10.1039/c7ra13744c

rsc.li/rsc-advances

Fabrication of perovskite solar cells (PSCs) in a simple way with high efficiency and stability remains a challenge. In this study, silver nanoparticles (Ag NPs) were sandwiched between two compact TiO_2 layers through a facile process of spin-coating an ethanolic $AgNO_3$ solution, followed by thermal annealing. The presence of Ag NPs in the electron-transporting layer of TiO_2 improved the light input to the device, the morphology of the perovskite film prepared on top, and eliminated leakage current. Photoluminescence and electron mobility studies revealed that the incorporation of Ag NPs in the ETL of the planar PSC device facilitated the electron–hole separation and promoted charge extraction and transport from perovskite to ETL. Hysteresis-free devices with incorporated Ag NPs gave a high average short-circuit current density (J_{sc}) of 22.91 ± 0.39 mA cm^{-2} and maximum power conversion efficiency of 17.25%. The devices also showed enhanced stability *versus* a control device without embedded Ag NPs. The possible reasons for the improvement are analyzed and discussed.

Open Access Article. Published on 19 February 2018. Downloaded on 2/12/2026 8:15:54 PM.
This article is licensed under a Creative Commons Attribution-NonCommercial 3.0 Unported Licence.

Introduction

One of the most challenging issues nowadays is getting sustainable, clean, and cheap energy sources because emissions from burning fossil fuels are widely recognized to be the cause of global warming and health problems. Solar energy is one of the most promising choices because of its abundance and being free of cost. It's the conversion of solar energy into electricity and its storage that are the primary tasks. Much progress has been made over the years through the developments in solar cells of various types in terms of their efficiency.[1] Yet for commercialization of these technologies, further improvements in efficiency, stability, and cost-reduction are needed.

Recently, perovskite materials are catching much attention of researchers for its potential application in solar cell.[2] Perovskite absorbs visible light, with a low and tuneable band gap of ~1.5 eV, high electron and hole mobility, which make it a good candidate as the active component in solar cells. Since the breakthrough report of Miyasaka *et al.* using perovskite as a visible light sensitizer for photoelectrochemical cells, giving 3.8% power conversion efficiency (PCE),[3] various advances have been made in device architecture and fabrication process, and most recently a high PCE of 21.1% has been reached for the perovskite-based solar cell.[2,4–13]

To further push for higher efficiency and ultimate commercialization of this technology, optimization of each component in the device has been tried, such as electron transporting layer (ETL), hole transporting layer (HTL), and electrode, besides the light-absorbing perovskite layer. In terms of ETL, a layer of mesoporous TiO_2 (mp-TiO_2) together with the compact TiO_2 (c-TiO_2) layer is necessary to reach the high efficiency reported.[14] Other metal oxides or metal-doped TiO_2 have been reported to modulate the electron-collecting or electron-transporting properties of the ETL.[15–29] Core–shell metallic nanoparticles (NPs) were also introduced in the meso-superstructure layer, with some improvements reported.[30,31] Metallic nanoparticles were explored for their unique absorption properties in the visible and near-IR region, as well as the plasmonic properties.[32] In particular, silver nanoparticles, Ag NPs, were incorporated in various ways in different layers of perovskite solar cells (PSCs) and beneficiary effects have been demonstrated.[33–39] Nevertheless, these devices usually involved more complicated preparation procedures, with little elaboration of the detailed mechanism.

In this work, we report the use of Ag NPs-embedded c-TiO_2 as ETL to improve the opto-electrical characteristics, charge

[a]*Institute of Chemistry, Academia Sinica, Nankang, Taipei 115, Taiwan. E-mail: ytt@gate.sinica.edu.tw*

[b]*Taiwan International Graduate Program (TIGP), Sustainable Chemical Science and Technology (SCST), Academia Sinica, Taipei, Taiwan*

[c]*Department of Applied Chemistry, National Chiao Tung University, Hsinchu, Taiwan*

[d]*Department of Chemistry, Nizam College, Osmania University, Hyderabad, India*

† Electronic supplementary information (ESI) available: Preparation of ETL, ETL full XPS spectra, UV-Vis absorption of ETL and perovskite, perovskite XRD, top view and cross-section SEM monograph, histogram *J–V* comparison and set of tables shows *J–V* characterization at least for 15 devices each. See DOI: 10.1039/c7ra13744c

Open Access Article. Published on 19 February 2018. Downloaded on 2/12/2026 8:15:54 PM.
This article is licensed under a Creative Commons Attribution-NonCommercial 3.0 Unported Licence.

extraction and transportation of planar PSCs with a device configuration of FTO/c-TiO_2/Ag NPs/c-TiO_2/perovskite ($CH_3NH_3PbI_3$)/Spiro-OMeTAD/Ag. The sandwiched Ag NPs were formed by a simple and robust spin-coating of ethanolic $AgNO_3$ solution on the c-TiO_2 layer and later annealed at high temperature. It was shown that the incorporation of Ag NPs in the centre of c-TiO_2 ETL layer promoted the formation of larger perovskite crystals with reduced grain boundaries, so that the electron trap density and the charge recombination pathways in the film were reduced. Also, the Ag NPs, with a specific amount, act as an electron scavenger and therefore electron-transporting nature of the TiO_2 layer was improved in the PSCs.

Experimental

Chemicals and materials

FTO (7 Ω) was purchased from UNI-ONWARD Corp. Titanium diisopropoxide bis(acetylacetonate) solution (75% in 2-propanol) and $AgNO_3$ (99.9999% trace metal basis) is obtained from Sigma-Aldrich. Perovskite precursors PbI_2 (99.9985%) were obtained from Alfa Aesar. The CH_3NH_3I (98%) and Spiro-OMeTAD were purchased from Lumtec. Li-TFSI was obtained from ACROS. 4-*tert*-Butylpyridine (TBP) was acquired from Ak Scientific Inc, and Ag slug (4 mm × 6 mm 99.9999%) was from Gredmann.

Experimental procedure

The FTO glass was cut into the size of 1.5 cm × 1.8 cm. A part of the FTO substrate (~4 mm) was etched with zinc powder and 2 N HCl. Then the substrate was cleaned by sonication in DI water, acetone, and 2-propanol respectively for 20 min and then dried in a flow of N_2 gas. The FTO substrate was treated by UV ozone for 30 min before device fabrication.

A solution of titanium diisopropoxide bis(acetylacetonate) was prepared by dissolving 55 μL stock solution of (75% in 2-propanol) in 1 mL 1-butanol to make 0.15 M solution. Spin-coating of this solution in a three-stage procedure (see ESI†) on the FTO substrate gave the single-layered c-TiO_2, double layered c-TiO_2 or Ag-embedded c-TiO_2. Double-layered c-TiO_2 was prepared by another spin-coating of c-TiO_2 on the single-layered TiO_2. To prepare Ag-sandwiched c-TiO_2, different concentrations of ethanolic $AgNO_3$ solutions (with drops of DI water added to dissolve $AgNO_3$) was spin-coated on the single layered c-TiO_2 and annealed at 130 °C for 10 min, followed by one additional spin-coating of the c-TiO_2 precursor on the Ag NP-covered c-TiO_2. Finally, all of the ETL layers were sintered at 500 °C for 30 min. Before coating perovskite layer, the ETL substrates were treated by UV–ozone for 30 min to clean the surface.

The perovskite precursor solution was prepared by following a one-step deposition procedure reported in the literature.[40] To a solution of DMSO (1 M) containing PbI_2 (1 M) and CH_3NH_3I (1 M), DMF (600 mg) is added and stirred at room temperature for 60 min. The precursor solution was passed through a 0.22 μm PVDF filter and then spin-coated on c-TiO_2/FTO substrate at 4000 rpm for 25 s. Diethyl ether was used to wash DMF away to give $CH_3NH_3I \cdot PbI_2 \cdot DMSO$ adduct. At the end of the spinning process, transparent perovskite film formed, which was converted to a thick black film after annealing for 2 min at 65 °C and 5 min at 100 °C.

For HTM, 40 mg Spiro-OMeTAD was dissolved in 0.5 mL chlorobenzene and 14.5 μL TBP, 7.5 μL Li-TFSI, and 14.5 μL FK209 were added successively. The solution was spin-coated on top of perovskite surface. Finally, 70–80 nm thick Ag metal was deposited as the terminal contact by thermal deposition at a pressure of 8×10^{-6} torr in a metal-masked area of 0.04 cm^2.

Characterization

The surface morphology and cross-section images of the devices were taken by field-emission scanning electron microscope (FE-SEM, ULTRA PLUS, a member of Carl Zeiss). Powder X-ray diffractions (XRDs) were recorded on a Bruker D8 Advance with Cu anode, $\lambda = 1.54060$ Å (angle range of $2\theta = 10°$ to 45°). PANCHUM PR-2000 (M) UV/VIS spectrophotometer was used to measure the UV-Vis absorption spectra of the perovskite. Steady-state photoluminescence spectra (PL) were taken at room temperature by FL920 (FLSP920 Edinburgh Photonics model) fluorimeter. Kratos Axis Ultra DLD was employed to obtain X-ray Photoelectron Spectroscopy (XPS) spectra. Atomic force microscopy analyses were carried out with a Multimode Atomic Force Microscope (Digital Instruments, Nanoscope III) using tapping mode with a silicon tip. *J–V* characteristics of PSCs were measured by Keithley 2400 digital source meter, under AM 1.5 G solar irradiation at 100 mW cm^{-2} (Newport, JIS C891, IEC 60904-9, ASTM E927-05 Class AAA) under 1 sun illumination with a scan rate of 0.01 V s^{-1}. The light intensity was determined by using a standard silicon photodiode (Hamamatsu S1133), calibrated by the National Renewable Energy Laboratory. The incident photon-to-current efficiency (IPCE) was measured by a system combining a xenon lamp, a monochromator, a chopper and a lock-in amplifier, together with a calibrated silicon photodetector. Both *J–V* and IPCE measurements were carried out at ambient condition without cell encapsulation on an area defined by a 0.04 cm^2 metal mask.

Results and discussion

The Ag NPs-embedded TiO_2 ETL was prepared by spin-coating ethanolic $AgNO_3$ solutions of different concentrations (1–20 mM) onto a pre-formed c-TiO_2/FTO layer, followed by another layer of c-TiO_2 layer and then annealed at 500 °C,[41] as detailed in the experimental procedure. The evidence of formation of Ag NPs from $AgNO_3$ within the TiO_2 layer after annealing was provided by XPS, XRD, and UV-Vis absorption spectroscopy. In the XPS measurement as shown in Fig. 1a (the full spectrum is presented in Fig. S1, ESI†), the deconvolution of Ag $3d_{5/2}$ and $3d_{3/2}$ signals gave binding energies at 368.0 and 374.1 eV respectively, which are consistent with previously published data for Ag NPs.[42] The powder XRD patterns for Ag NPs-embedded ETL (Fig. 1b) revealed diffraction peaks at 2θ values of 38.2°, 44.3°, 64.7° and 77.4°, corresponding to that for (111), (200), (220), and (311) planes, and suggest the formation

 This journal is © The Royal Society of Chemistry 2018

Open Access Article. Published on 19 February 2018. Downloaded on 2/12/2026 8:15:54 PM.
This article is licensed under a Creative Commons Attribution-NonCommercial 3.0 Unported Licence.

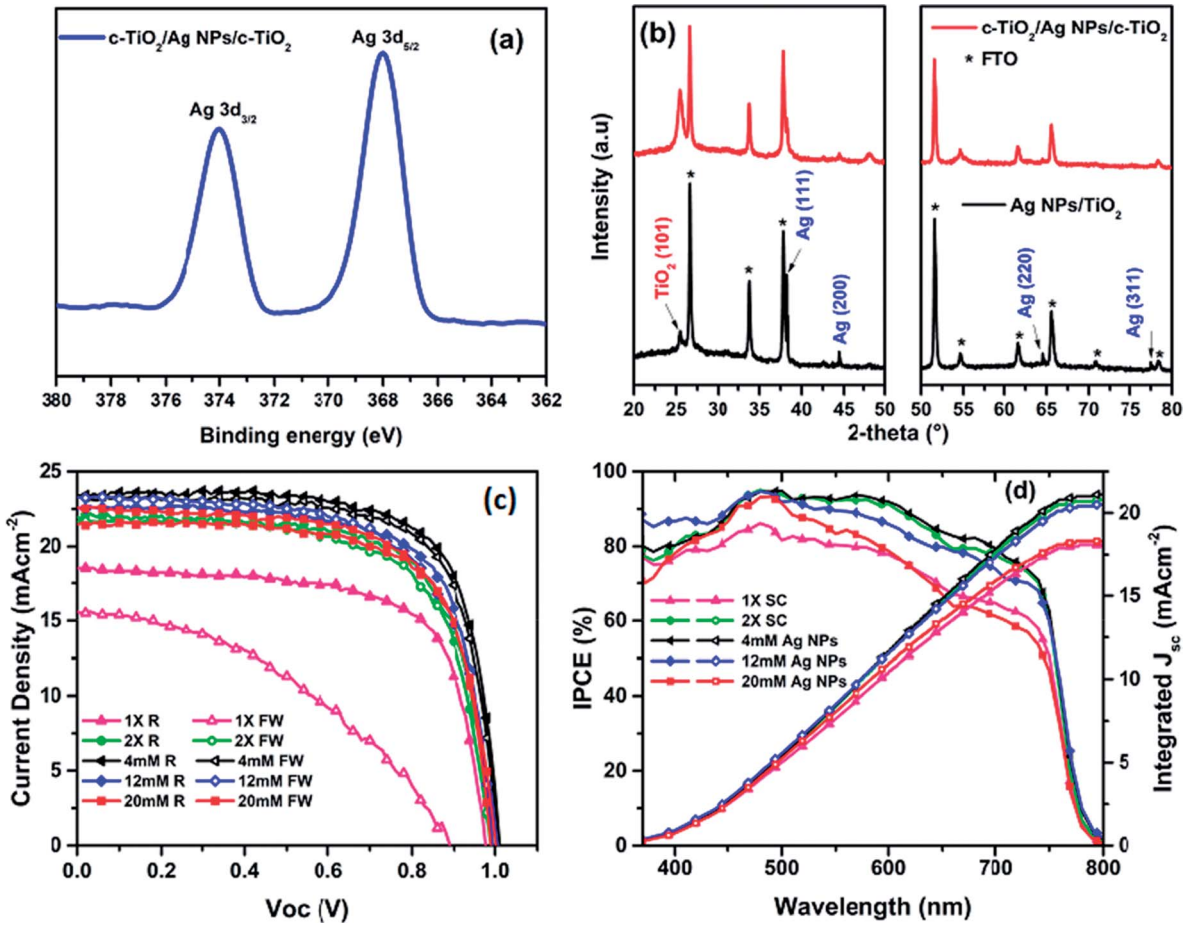

Fig. 1 (a) XPS spectra of c-TiO_2/Ag NPs (4 mM)/c-TiO_2 prepared on FTO substrate (b) XRD of Ag NPs (4 mM)/c-TiO_2 and c-TiO_2/Ag NPs (4 mM)/c-TiO_2 prepared on FTO, (c) reverse and forward sweep J–V characteristics (d) IPCE spectra and integrated J_{sc} of planar PSCs prepared form control and Ag NPs embedded ETLs.

of pure face-centered cubic Ag NPs, with no other phases present.[43]

The UV-Vis absorption spectra (Fig. S2a, ESI†) revealed the absorption edge for pristine c-TiO_2 shifted from 387 nm for the single layer c-TiO_2 toward around 413 nm for the Ag NPs-embedded c-TiO_2 layers, presumably due to the incorporation of Ag NPs, which is known to give UV absorption above 400 nm.[37,44–46] Importantly, the TiO_2 ETL embedding Ag NPs showed stronger UV-Vis absorption compared to the pristine c-TiO_2, which may be the result of Surface Plasmon Resonance (SPR) of Ag NPs. All the aforementioned characterizations confirmed that Ag NPs were successfully formed in between the c-TiO_2 layers. The optical transmittance of ETL is an important criterion to prepare high efficiency PSCs. So that, the optical transmittances are recorded for 1× SC, 2× SC and 4 mM Ag NPs-embedded TiO_2 layers (Fig. S2b, ESI†). About 80% transmittance was recorded for all of the samples, which indicates that the incorporation of adequate amount Ag NPs insignificantly change the transmittance of the TiO_2 film. With the Ag NPs in place, planar perovskite solar cells were then fabricated by spin-coating perovskite layer on top of various ETLs prepared under the same condition, followed by spin-coating Spiro-OMeTAD and depositing Ag back electrode to complete the device structure. A preliminary survey of the effect of incorporating Ag NPs on device performance was carried out, with the Ag NPs prepared from aqueous $AgNO_3$ solutions of 1 mM to 20 mM concentrations. As a reference cell, TiO_2 layers by spin-coating once and twice were also used. Abbreviations of 1× SC, 2× SC, 2× SC $AgNO_3$ (x mM) are used to represent devices with single spin-coating, double spin-coating, and double spin-coating with embedded Ag NPs obtained from x mM $AgNO_3$ solution respectively. The results showed that better performances were obtained with low concentration $AgNO_3$ solutions and peaked for that from 4 mM $AgNO_3$ solution.

Thus the device with 2× SC Ag NPs (4 mM) as ETL showed a maximum PCE of 17.25%, an open-circuit voltage (V_{oc}) of 1.01 V, short-circuit current density (J_{sc}) of 23.36 mA cm^{-2}, and a fill factor (FF) of 73.11% (Fig. 1c, Table 1). However, when 2× SC Ag NPs (12 mM, and 20 mM) were used as ETL, the device PCE decreased to 15.92% and 15.26% respectively with decreased J_{sc} and FF. In contrast, the reference solar cells fabricated by using 1× SC and 2× SC TiO_2 as ETL showed smaller PCE than the 2× SC Ag NPs (4 mM) device, at 12.35% and 15.17% respectively. Compared to the others, the 1× SC

Open Access Article. Published on 19 February 2018. Downloaded on 2/12/2026 8:15:54 PM.
This article is licensed under a Creative Commons Attribution-NonCommercial 3.0 Unported Licence.

Table 1 Summary of the photovoltaics performances for 1× SC, 2× SC and 2× SC Ag NPs (4 mM, 12 mM and 20 mM) ETL-based PSCs. Values inside and outside of the brackets are the best device performances and average device performances for at least for 15 devices respectively

Method	V_{oc} (V)	J_{sc} (mA cm^{-2})	FF (%)	PCE (%)	R_{sh} (KΩ cm^{-2})	R_s (Ω cm^{-2})
1× SC	0.95 ± 0.02 (0.98)	16.76 ± 1.37 (18.47)	68.90 ± 2.64 (68.20)	11.02 ± 1.01 (12.35)	0.35	6.27
2× SC	0.99 ± 0.01 (0.98)	21.79 ± 0.50 (21.95)	69.33 ± 1.46 (70.51)	14.91 ± 0.43 (15.17)	1.67	4.76
Ag NPs (4 mM)	1.00 ± 0.01 (1.01)	22.91 ± 0.39 (23.36)	71.40 ± 1.81 (73.11)	16.37 ± 0.32 (17.25)	6.02	2.87
Ag NPs (12 mM)	0.99 ± 0.01 (0.99)	22.40 ± 0.59 (22.52)	67.82 ± 1.85 (71.41)	15.03 ± 0.43 (15.92)	3.12	3.34
Ag NPs (20 mM)	0.99 ± 0.01 (1.00)	21.09 ± 1.06 (21.62)	68.35 ± 2.54 (67.44)	14.23 ± 0.68 (15.26)	0.57	4.43

device also had very low PCE for the forward sweep (5.80%), suggesting this device had substantial hysteresis, an undesirable situation in device operation. This phenomenon was eliminated for devices with TiO_2 embedding Ag NPs, particularly for the 2× SC Ag NPs (4 mM) device (Table S1, ESI†).

The PCE for the 2× SC device also improved over that for 1× SC device, to a maximum of 15.17%. This means *ca.* 23% improvement over the pristine 1× SC-based device. The possible reason for the improved performance could be a better c-TiO_2 coverage on FTO layer when a second c-TiO_2 layer was employed. This would reduce the possible direct contacts between perovskites and FTO, which is expected to decrease the chance of charge separation and increase recombination for the excited perovskites. However, 2× SC devices showed higher series resistance (R_s) and much smaller shunting resistance (R_{sh}), compared to the Ag NPs-incorporated PSCs. As shown in Table 1, the R_s for 2× SC (*ca.* 4.76 Ω cm^{-2}) device is about two folds higher than that with 2× SC Ag NPs (4 mM) device (*ca.* 2.87 Ω cm^{-2}). A higher R_s would suggest lower electron mobility for the device without Ag NPs-embedded, as will be discussed later. The same phenomena were observed for R_{sh} measurement, which quantifies explicitly the degree of recombination at the interface and relates to photocurrent loss.[47] The device with 2× SC Ag NPs (4 mM) showed a R_{sh} value of 6020 Ω cm^{-2}, which is more than three-fold photocurrent loss resistance than that with 2× SC (1670 Ω cm^{-2}). This suggests that in the device fabricated with Ag NPs (4 mM) ETL, the photogenerated charge carriers are successfully separated and transported by suppressing charge recombination at the interfaces and resulting in a higher PCE. The R_s and R_{sh} properties were improved for nearly all of the Ag NPs-embedding devices compared to 1× SC and 2× SC devices, although when the amount of Ag NPs increased by using 12 mM and 20 mM solution, the series resistance started to build up and R_{sh} decreased to 3120 Ω cm^{-2} and 570 Ω cm^{-2} respectively, resulting in a decrease in performances of the cells. The box charts in Fig. 2 summarize the photovoltaics performance characteristics for devices prepared on various TiO_2 substrates. Apparently, the highest J_{sc} values were recorded for devices prepared from that with 2× SC Ag NPs (4 mM) ETL, so were the PCEs for these devices. The histogram in Fig. S3, ESI† also showed the average PCE and their corresponding V_{oc}, J_{sc}, FF for at least 15 devices each for 1× SC, 2× SC and 2× SC Ag NPs (4 mM)-based ETL and confirmed the high reproducibility of the performance characteristics. Thus there is ~39% and ~14% PCE enhancement for devices prepared from the 2× SC Ag NPs (4 mM)-based device over the pristine 1× SC and 2× SC respectively.

That the incorporation of Ag NPs in the TiO_2 layer has a beneficiary effect on the device performance is further confirmed by additional evidences as described below. The incident photon-to-current efficiency (IPCE) mainly depends on the average size of the perovskite crystals, grain boundaries, and perovskite thickness, which influence the light harvesting efficiency (η_{lhe}), exciton diffusion efficiency (η_{ed}), charge separation efficiency (η_{cs}), and charge collection efficiency (η_{cc}).[48] The IPCE of the control and Ag NPs-embedded cells are presented in Fig. 1d. It can be seen that Ag NPs (4 mM)-embedded device having the highest integrated J_{sc} gave a maximum IPCE% of ~88% at *ca.* 495 nm and the highest IPCE% in the broad wavelength range from 450 nm to 750 nm compared to the other ETLs. However, the Ag NPs embedded ETL showed a little absorbance enhancement at about 450–600 nm, the IPCE improvement is all over the 400–800 nm range. As a result of incorporation of Ag NPs, the light absorption of perovskite increased not only in a specific region but also in all panchromatic wavelength ranges so that the IPCE is influenced accordingly. The same phenomena are observed when Ag and Au core shall metallic nanoparticles are incorporated in ETL of perovskite solar cell.[30,31] The rather flat spectral profile and high IPCE% led to outstanding light harvesting efficiency. Whereas, the control device with 1× SC and 2× SC TiO_2 showed ~78% and 86% IPCE respectively at the same wavelength. When the amount of Ag NPs increased, the IPCE% decreased. Thus similar trend as the PCE results is followed for respective devices. The integrated J_{sc} value is

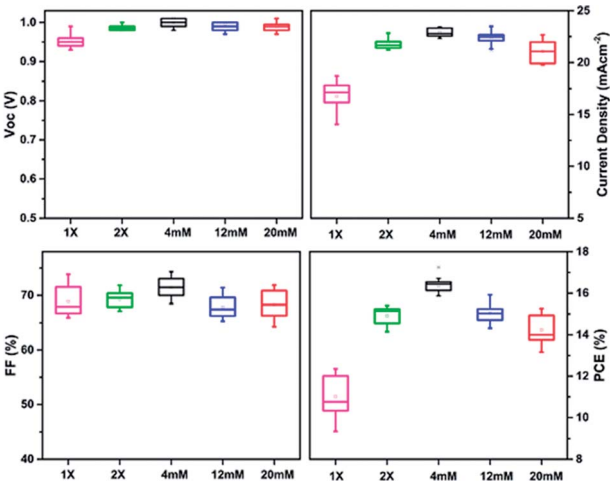

Fig. 2 Box chart comparison of photovoltaics parameters for 1× SC, 2× SC and Ag NPs (4 mM, 12 mM and 20 mM) ETL-based planar PSCs.

This journal is © The Royal Society of Chemistry 2018

Open Access Article. Published on 19 February 2018. Downloaded on 2/12/2026 8:15:54 PM.
This article is licensed under a Creative Commons Attribution-NonCommercial 3.0 Unported Licence.

presented in double Y axis figure for IPCE in Fig. 1d, and integrated J_{sc} values of 18.1 mA cm^{-2}, 20.8 mA cm^{-2}, 21.1 mA cm^{-2}, 20.5 mA cm^{-2} and 18.1 mA cm^{-2} are extracted for 1× SC, 2× SC, 4 mM Ag NPs-, 12 mM Ag NPs- and 20 mM Ag NPs-incorporated TiO_2 films respectively. A small discrepancy (~2–9.6%) was observed between the J_{sc} measured from J–V and J_{sc} integrated from IPCE because the latter measurement was carried out in a single wavelength with much lower intensity than the one sun radiation.[49,50]

In order to understand the root cause for suppressed PCE when increasing Ag NPs concentration in the ETL, the top view SEM images for the perovskite films grown on respective ETLs were taken. As shown in Fig. 3a–c, the top-view SEM images of perovskite films on 1× SC, 2× SC, and Ag NPs (4 mM) ETLs are different in terms of surface morphology. Grains in the perovskite film grown on 2× SC Ag NPs (4 mM) TiO_2 were bigger compared to that on 1× SC and 2× SC TiO_2. The grains in films on 2× SC Ag NP (12 mM and 20 mM) had similar crystal size as for Ag NP (4 mM), but more cracks appeared, particularly for Ag NP (20 mM) (Fig. S4a and b, ESI†). It is intriguing that the Ag NPs buried within c-TiO_2 layer would affect the morphology of perovskite deposited on top. Considering the surface energy of a substrate would affect the morphology of a film formed on top, we measured the water contact angle on various c-TiO_2 surfaces (Fig. 3e–g). The same treatment of 30 min UV–ozone exposure was applied to all of the ETLs before measuring contact angles. The water contact angle value on 1× SC and 2× SC TiO_2 had a value of <5°, which suggests a highly wettable surface. However, the water contact angle on Ag NPs (4 mM), Ag NPs (12 mM) and Ag NPs (20 mM) TiO_2 increased to ~10.5°, ~15° and ~22° respectively. These may suggest that a delicate dependence of grain size on the wettability, smaller and continuous grains for highly wettable surfaces and yet cracks appearing for less wettable surfaces. Previous reports on wettability of the solid surface showed that the roughness of a solid surface will have an effect on wetting property in that a rougher surface tend to be more wettable.[51] Our AFM micrographs show that 1× SC has the highest roughness (26.1 nm) and it showed high wettability with a contact angle of less than 5°. The surface roughness decreased to 23.0 nm for 2× SC, and

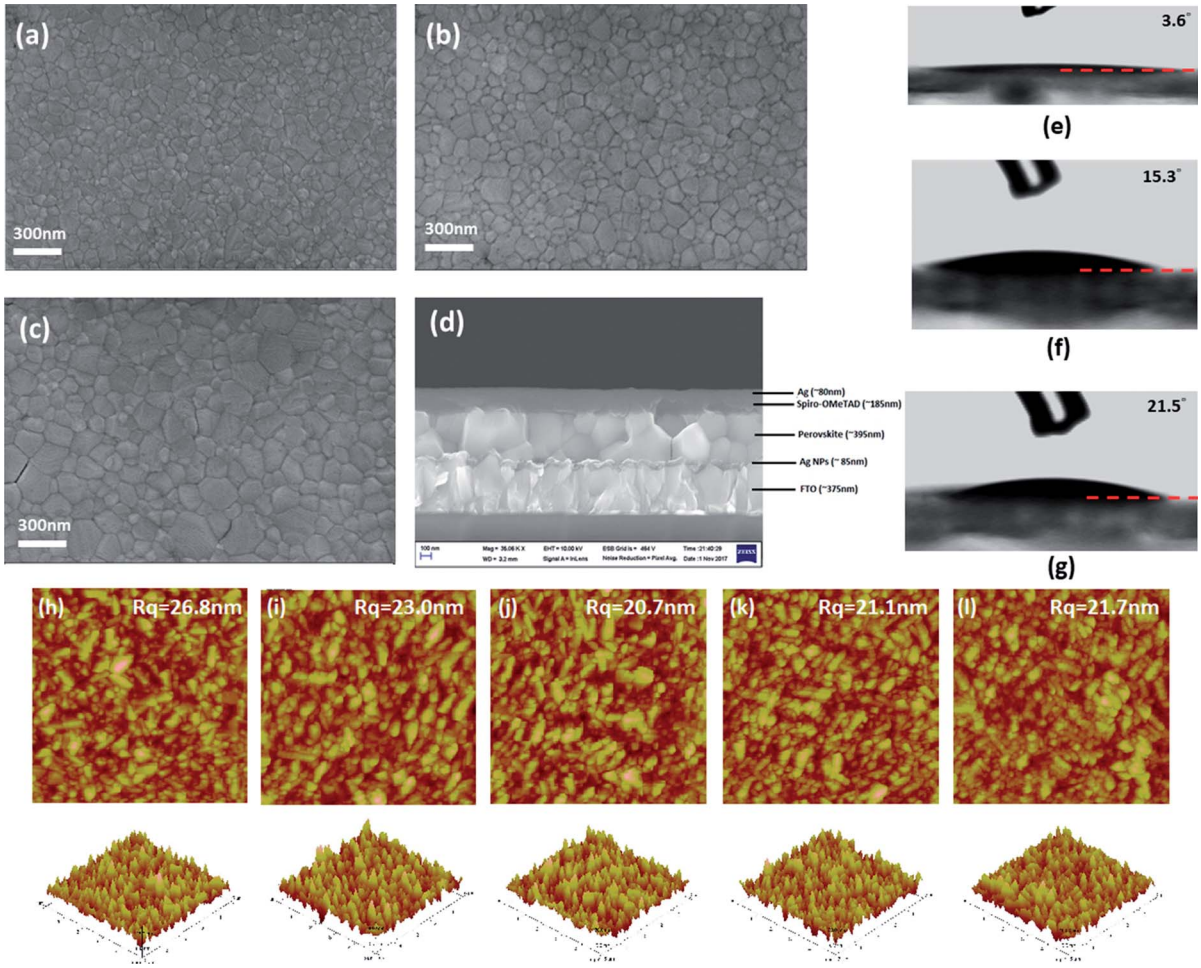

Fig. 3 Top view SEM images of (a–c) perovskite films prepared on 1× SC, 2× SC and Ag NPs (4 mM) ETL, (d) cross-section SEM image of perovskite device with a structure of FTO/Ag NPs (4 mM)/perovskite/Spiro-OMeTAD/Ag, water contact angle (e–g) on 1× SC, Ag NPs (12 mM)- and Ag NPs (20 mM)-embedded TiO_2 surfaces after 30 min UV–ozone treatment, (h–l) AFM surface and corresponding 3-dimentional images (bottom) of ETL films prepared from 1× SC, 2× SC, 4 mM Ag NPs, 12 mM Ag NPs and 20 mM Ag NPs respectively (all scans are 5 μm × 5 μm).

Open Access Article. Published on 19 February 2018. Downloaded on 2/12/2026 8:15:54 PM.
This article is licensed under a Creative Commons Attribution-NonCommercial 3.0 Unported Licence.

a lower surface roughness was observed for all Ag NPs-incorporated surfaces, with a least roughness of 20.7 nm for 4 mM Ag NPs-embedded film. The perovskite film coated on the rougher surface (thus more wettable surface) gave smaller grain size because of more nucleation sites present on the rougher surface. A smoother ETL will induce the growth of larger grains of perovskite layer.

The thickness of 1× SC, 2× SC and Ag NPs (4 mM) TiO_2 were measured by cross-sectional SEM and the results are presented in (Fig. S4c and d, ESI† and Fig. 3d), with an ETL thickness of ~50 nm, ~90 nm, and ~95 nm respectively. The perovskite layer thickness grown on different underneath layers were slightly different, at ~340 nm, ~350 nm, and ~395 nm on 1× SC, 2× SC, and 2× SC Ag NPs (4 mM) TiO_2 respectively. The top view and cross-sectional SEM micrographs suggested a certain level of roughness increased the thickness and improved the morphology of the perovskite film formed on top and contributed to the performance of the device recorded.[52]

UV-Vis and XRD were recorded for perovskite films grown on 1× SC, 2× SC and 2× SC Ag NPs (4 mM) ETL layers (Fig. S5a, ESI†). The active perovskite layer prepared in our process absorbed light in UV-Vis range with an absorption band edge *ca.* 770 nm, which is in agreement with the previous report.[53] UV-Vis absorbing for Ag NPs (4 mM) showed a little improvement in the whole range of UV-Vis compared to 1× SC and 2× SC. The powder XRD spectra (Fig. S5b, ESI†) presented dominant peaks at 2θ of 14.2° (110) and 28.5° (220) for perovskite, with no traces for either PbI_2 or CH_3NH_3I, indicating the formation of high quality and pure perovskite crystal over the ETLs. There is nevertheless little difference in the UV-Vis and PXRD results for perovskite on these c-TiO_2 ETLs, probably because the amount of Ag NPs embedded is small.

Photoluminescence and electron mobility studies were carried out to understand the characteristics of charge separation and transportation in these devices. Thus the steady-state photoluminescence (PL) was measured on half devices of perovskite/ETLs/FTO with 1× SC, 2× SC and 2× SC Ag NPs (4 mM) TiO_2 as ETL. As shown in Fig. 4, the PL spectrum of perovskite on a bare glass substrate showed a strong emission at ~774 nm. Much reduced PL intensity was recorded for perovskite grown on 2× SC Ag NPs (4 mM) ETL. This presumably could indicate a suppressed charge recombination in the Ag NP-embedded film as compared to that on 1× SC and 2× SC ETL films. This suggests a higher chance of charge separation and transportation to the electrodes when the 2× SC Ag NP (4 mM) TiO_2 is used as ETL. This is in agreement with the R_s and R_{sh} measurements of the prepared devices.

In order to confirm the influence of Ag NPs on charge carrier transport, electron-only device with a device configuration of FTO/c-TiO_2/Ag NPs/c-TiO_2/perovskite/Al (65 nm) was prepared, and the *J*–*V* characteristics were measured in the dark to determine electron mobility of the device. Mott–Gurney law is used to define Space-Charge-Limited Current (SCLC) region, with $J = 9/8\varepsilon_o\varepsilon_r E^2/L$, where J is the current density, E is electric field, ε_o is permittivity of the vacuum (8.854×10^{-12} F m^{-1}), ε_r is the relative dielectric constant of $CH_3NH_3PbI_3$ ($\varepsilon_r = 32$),[54] and L is perovskite film thickness (1× ST = ~330 nm, 2× SC = ~350 nm and 2× SC Ag NP (4 mM) = ~395 nm).[14,45] The mobility is dependent on the electric field and can be expressed by a Poole–Frenkel equation $\mu(E) = \mu_o \exp(\beta E^{1/2})$, where μ_o is the zero-field mobility and β is Poole–Frenkel factor. The slope (β) and intercept zero-field mobility (μ_o) were obtained from the plot of $\ln(JE^{-2})$ *versus* $E^{1/2}$.[55] The SCLC electron mobilities calculated are presented in Fig. 5. The device fabricated with Ag NPs (4 mM)-embedded TiO_2 showed an electron mobility of 2.57 × 10^{-4} cm^2 V^{-1} s^{-1}, which is significantly higher than that with 1× SC (1.46 × 10^{-4} cm^2 V^{-1} s^{-1}) and 2× SC (2.03 × 10^{-4} cm^2 V^{-1} s^{-1}). This suggested the Ag NPs-incorporated ETL facilitated the charge extraction and prevent electron and hole recombination more than that with 1× SC and 2× SC ETLs. This also matched with the PL and charge resistance studies.

Finally, the long-term stability, which is one of the essential criteria for PSCs commercialization, was studied for devices with 1× SC, 2× SC and 2× SC Ag NPs (4 mM) as ETLs. Devices were stored in a dry box and only taken out for measurements in the atmosphere without encapsulation. The results are presented in Fig. 6, which revealed that PSC with 2× SC Ag NPs (4 mM) ETL retained *ca.* 89% of its initial PCE after 28 days,

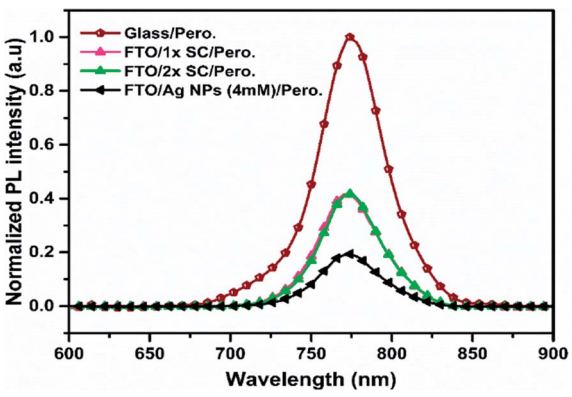

Fig. 4 Normalized PL spectra of perovskite thin films prepared on glass, 1× SC ETL, 2× SC ETL and c-TiO_2/Ag NPs (4 mM)/c-TiO_2 ETLs.

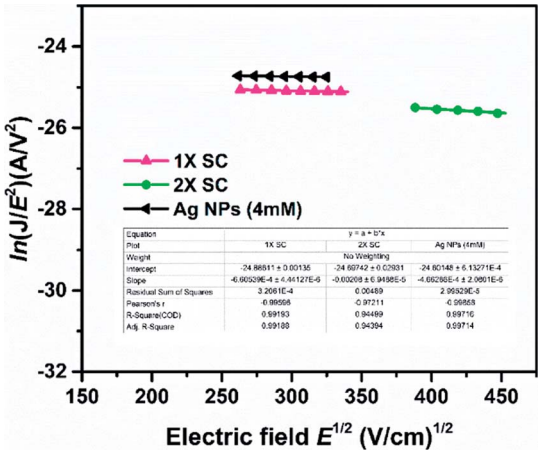

Fig. 5 Measurement of electron mobility by SCLC method at dark *J*–*V* characteristics for devices with and without the presence of Ag NPs.

This journal is © The Royal Society of Chemistry 2018

Open Access Article. Published on 19 February 2018. Downloaded on 2/12/2026 8:15:54 PM.
This article is licensed under a Creative Commons Attribution-NonCommercial 3.0 Unported Licence.

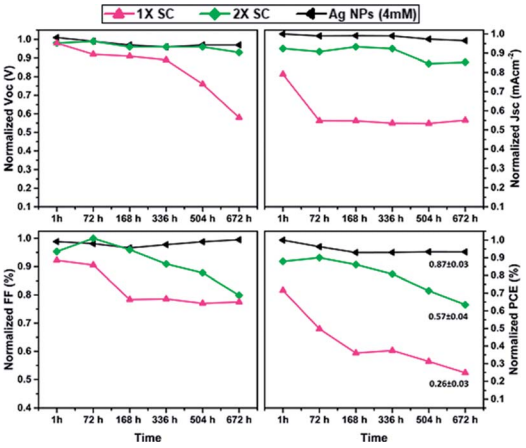

Fig. 6 Long term stability test for 1× SC, 2× SC and Ag NPs (4 mM) ETL based-PSCs without encapsulation for 28 days. The dotted lines represent the maximum values for all device. The standard deviation in the normalized PCE box chart showed the average percentage retained at least for 5 devices.

whereas that with 1× SC and 2× SC ETL degraded and retained ~32% and ~62% of their initial PCEs respectively after the same period. Also shown are the stability of other parameters like V_{oc}, J_{sc}, and FF. The possible reason for better stability for Ag NPs (4 mM) may be the formation of bigger crystal with less grain boundaries so that the intrusion of moisture in the cell can be decreased.

Conclusions

In summary, we demonstrated a new and cheaper approach to tune the ETL of the perovskite solar cell by incorporating Ag NPs inside the compact TiO_2 layer through annealing $AgNO_3$ salt deposited in the middle of the layer. Smooth and compact perovskite film was formed in the presence of Ag NPs, which improved the film morphology, electron extraction, and transport properties, as evidenced by SEM, PL and SCLC measurements. Higher electron mobility, J_{sc}, and FF, thus higher PCE were obtained when an adequate amount of Ag NPs was embedded in the TiO_2 layer. Presumably, the growth of large crystals with fewer grain boundaries on Ag NPs-embedded ETLs improves the J_{sc} and FF of the device by suppressing series resistance and enhance shunting resistance and also contributed to the long-term stability for the prepared device.

Conflicts of interest

There are no conflicts to declare.

Acknowledgements

The authors wish to thank the financial support of Ministry of Science and Technology, Taiwan (Grant number: 106-2113-M-001-003) and SERB, India.

Notes and references

1 X. Fan, M. Zhang, X. Wang, F. Yang and X. Meng, *J. Mater. Chem. A*, 2013, **1**, 8694.
2 P. Gao, M. Grätzel and M. K. Nazeeruddin, *Energy Environ. Sci.*, 2014, **7**, 2448.
3 A. Kojima, K. Teshima, Y. Shirai and T. Miyasaka, *J. Am. Chem. Soc.*, 2009, **131**, 6050.
4 M. Saliba, T. Matsui, J.-Y. Seo, K. Domanski, J.-P. Correa-Baena, M. K. Nazeeruddin, S. M. Zakeeruddin, W. Tress, A. Abate and A. Hagfeldt, *Energy Environ. Sci.*, 2016, **9**, 1989.
5 N. J. Jeon, J. H. Noh, Y. C. Kim, W. S. Yang, S. Ryu and S. I. Seok, *Nat. Mater.*, 2014, **13**, 897.
6 J.-H. Im, I.-H. Jang, N. Pellet, M. Grätzel and N.-G. Park, *Nat. Nanotechnol.*, 2014, **9**, 927.
7 M. Liu, M. B. Johnston and H. J. Snaith, *Nature*, 2013, **501**, 395.
8 Q. Chen, H. Zhou, Z. Hong, S. Luo, H.-S. Duan, H.-H. Wang, Y. Liu, G. Li and Y. Yang, *J. Am. Chem. Soc.*, 2013, **136**, 622.
9 W. Nie, H. Tsai, R. Asadpour, J.-C. Blancon, A. J. Neukirch, G. Gupta, J. J. Crochet, M. Chhowalla, S. Tretiak and M. A. Alam, *Science*, 2015, **347**, 522.
10 K. M. Boopathi, M. Ramesh, P. Perumal, Y.-C. Huang, C.-S. Tsao, Y.-F. Chen, C.-H. Lee and C.-W. Chu, *J. Mater. Chem. A*, 2015, **3**, 9257.
11 T. Salim, S. Sun, Y. Abe, A. Krishna, A. C. Grimsdale and Y. M. Lam, *J. Mater. Chem. A*, 2015, **3**, 8943.
12 T.-B. Song, Q. Chen, H. Zhou, C. Jiang, H.-H. Wang, Y. M. Yang, Y. Liu, J. You and Y. Yang, *J. Mater. Chem. A*, 2015, **3**, 9032.
13 G. Yang, H. Tao, P. Qin, W. Ke and G. Fang, *J. Mater. Chem. A*, 2016, **4**, 3970.
14 M. Abdi-Jalebi, M. I. Dar, A. Sadhanala, S. P. Senanayak, F. Giordano, S. M. Zakeeruddin, M. Grätzel and R. H. Friend, *J. Phys. Chem. Lett.*, 2016, **7**, 3264.
15 Q. Dong, Y. Shi, K. Wang, Y. Li, S. Wang, H. Zhang, Y. Xing, Y. Du, X. Bai and T. Ma, *J. Phys. Chem. C*, 2015, **119**, 10212.
16 Z. Zhu, X. Zheng, Y. Bai, T. Zhang, Z. Wang, S. Xiao and S. Yang, *Phys. Chem. Chem. Phys.*, 2015, **17**, 18265.
17 M. A. Mejía Escobar, S. Pathak, J. Liu, H. J. Snaith and F. Jaramillo, *ACS Appl. Mater. Interfaces*, 2017, **9**, 2342.
18 D. Bi, G. Boschloo, S. Schwarzmüller, L. Yang, E. M. Johansson and A. Hagfeldt, *Nanoscale*, 2013, **5**, 11686.
19 M. H. Kumar, N. Yantara, S. Dharani, M. Graetzel, S. Mhaisalkar, P. P. Boix and N. Mathews, *Chem. Commun.*, 2013, **49**, 11089.
20 D.-Y. Son, J.-H. Im, H.-S. Kim and N.-G. Park, *J. Phys. Chem. C*, 2014, **118**, 16567.
21 M.-C. Wu, S.-H. Chan, M.-H. Jao and W.-F. Su, *Sol. Energy Mater. Sol. Cells*, 2016, **157**, 447.
22 B. Zhao, X. Wen, M. Jiang, J. Wu, F. Lan, J. Wang, D. den Engelsen, G. Li and D. Gao, *J. Mater. Chem. A*, 2017, **5**, 3691.
23 X. Zhao, H. Shen, Y. Zhang, X. Li, X. Zhao, M. Tai, J. Li, J. Li, X. Li and H. Lin, *ACS Appl. Mater. Interfaces*, 2016, **8**, 7826.
24 D.-B. Li, L. Hu, Y. Xie, G. Niu, T. Liu, Y. Zhou, L. Gao, B. Yang and J. Tang, *ACS Photonics*, 2016, **3**, 2122.

Open Access Article. Published on 19 February 2018. Downloaded on 2/12/2026 8:15:54 PM.
This article is licensed under a Creative Commons Attribution-NonCommercial 3.0 Unported Licence.

25 S.-G. Chen, S. Chappel, Y. Diamant and A. Zaban, *Chem. Mater.*, 2001, **13**, 4629.
26 M. Yang, R. Guo, K. Kadel, Y. Liu, K. O'Shea, R. Bone, X. Wang, J. He and W. Li, *J. Mater. Chem. A*, 2014, **2**, 19616.
27 D. H. Kim, G. S. Han, W. M. Seong, J. W. Lee, B. J. Kim, N. G. Park, K. S. Hong, S. Lee and H. S. Jung, *ChemSusChem*, 2015, **8**, 2392.
28 F. Giordano, A. Abate, J. P. C. Baena, M. Saliba, T. Matsui, S. H. Im, S. M. Zakeeruddin, M. K. Nazeeruddin, A. Hagfeldt and M. Graetzel, *Nat. Commun.*, 2016, **7**, 10379.
29 J. Wang, M. Qin, H. Tao, W. Ke, Z. Chen, J. Wan, P. Qin, L. Xiong, H. Lei and H. Yu, *Appl. Phys. Lett.*, 2015, **106**, 121104.
30 M. Saliba, W. Zhang, V. M. Burlakov, S. D. Stranks, Y. Sun, J. M. Ball, M. B. Johnston, A. Goriely, U. Wiesner and H. J. Snaith, *Adv. Funct. Mater.*, 2015, **25**, 5038.
31 W. Zhang, M. Saliba, S. D. Stranks, Y. Sun, X. Shi, U. Wiesner and H. J. Snaith, *Nano Lett.*, 2013, **13**, 4505.
32 P. Wang, D. Tanaka, S. Ryuzaki, S. Araki, K. Okamoto and K. Tamada, *Appl. Phys. Lett.*, 2015, **107**, 151601.
33 Y. Liu, F. Lang, T. Dittrich, A. Steigert, C.-H. Fischer, T. Köhler, P. Plate, J. Rappich, M. C. Lux-Steiner and M. Schmid, *RSC Adv.*, 2017, **7**, 1206.
34 D. Yang, J. G. Jang, J. Lim, J.-K. Lee, S. H. Kim and J.-I. Hong, *ACS Appl. Mater. Interfaces*, 2016, **8**, 21522.
35 G. Kakavelakis, K. Alexaki, E. Stratakis and E. Kymakis, *RSC Adv.*, 2017, **7**, 12998.
36 J. Huang, M. Wang, L. Ding, F. Igbari and X. Yao, *Sol. Energy*, 2016, **130**, 273.
37 H. Nourolahi, A. Behjat, S. H. Zarch and M. Bolorizadeh, *Sol. Energy*, 2016, **139**, 475.
38 S. Li, J. Hu, Y. Yang, L. Zhao, Y. Qiao, W. Liu, P. Liu and M. Chen, *Appl. Phys. A: Mater. Sci. Process.*, 2017, **123**, 628.
39 G. M. Kim and T. Tatsuma, *J. Phys. Chem. C*, 2017, **121**, 11693.
40 N. Ahn, D.-Y. Son, I.-H. Jang, S. M. Kang, M. Choi and N.-G. Park, *J. Am. Chem. Soc.*, 2015, **137**, 8696.
41 L. Qu, G. Shi, X. Wu and B. Fan, *Adv. Mater.*, 2004, **16**, 1200.
42 D. Mott, N. T. Thuy, Y. Aoki and S. Maenosono, *Philos. Trans. R. Soc., A*, 2010, **368**, 4275.
43 K. Shameli, M. B. Ahmad, A. Zamanian, P. Sangpour, P. Shabanzadeh, Y. Abdollahi and M. Zargar, *Int. J. Nanomed.*, 2012, **7**, 5603.
44 S. K. Kuriechen, S. Murugesan and S. P. Raj, *J. Catal.*, 2013, **2013**, 1.
45 G. Yin, J. Ma, H. Jiang, J. Li, D. Yang, F. Gao, J. Zeng, Z. Liu and S. F. Liu, *ACS Appl. Mater. Interfaces*, 2017, **9**, 10752.
46 C. F. Bohren and D. R. Huffman, *Absorption and scattering of light by small particles*, John Wiley & Sons, 2008.
47 H.-K. Lin, Y.-W. Su, H.-C. Chen, Y.-J. Huang and K.-H. Wei, *ACS Appl. Mater. Interfaces*, 2016, **8**, 24603.
48 J. H. Heo, M. H. Lee, M. H. Jang and S. H. Im, *J. Mater. Chem. A*, 2016, **4**, 17636.
49 J. A. Christians, J. S. Manser and P. V. Kamat, *J. Phys. Chem. Lett.*, 2015, **6**, 852.
50 E. Zimmermann, P. Ehrenreich, T. Pfadler, J. A. Dorman, J. Weickert and L. Schmidt-Mende, *Nat. Photonics*, 2014, **8**, 669.
51 R. N. Wenzel, *Ind. Eng. Chem.*, 1936, **28**, 988.
52 T. S. Sherkar, C. Momblona, L. Gil-Escrig, J. Ávila, M. Sessolo, H. J. Bolink and L. J. A. Koster, *ACS Energy Lett.*, 2017, **2**, 1214.
53 U. Thakur, U. Kwon, M. M. Hasan, W. Yin, D. Kim, N. Y. Ha, S. Lee, T. K. Ahn and H. J. Park, *Sci. Rep.*, 2017, **7**, 43979.
54 F. Cai, L. Yang, Y. Yan, J. Zhang, F. Qin, D. Liu, Y.-B. Cheng, Y. Zhou and T. Wang, *J. Mater. Chem. A*, 2017, **5**, 9402.
55 S. B. Mane, A. A. Sutanto, C.-F. Cheng, M.-Y. Xie, C.-I. Chen, M. Leonardus, S.-C. Yeh, B. B. Beyene, E. W.-G. Diau and C.-T. Chen, *ACS Appl. Mater. Interfaces*, 2017, **9**, 31950.

This journal is © The Royal Society of Chemistry 2018